Control of fault geometry, interaction and mechanical stratigraphy on strain distribution in normal fault zones

LAPADAT, IOAN,ALEXANDRU

Control of fault geometry and mechanical stratigraphy on normal fault-related folding: a case study from Inner Moray Firth Basin

Alexandru Lăpădat[1], Jonathan Imber[1,2], Ken McCaffrey[1], Graham Yielding[2], Jonathan Long[3], Richard Jones[3]

[1]*Department of Earth Sciences, Durham University, Durham, DH1 3LE, UK*
[2]*Badley Geoscience Ltd., Hundleby, Spilsby, Lincolnshire, PE23 5NB, UK*
[3]*Geospatial Research Ltd., Suites 7 & 8, Harrison House, Hawthorne Terrace, Durham, DH1 4EL, UK*

Introduction

The volume of rock surrounding a normal fault or a normal fault array typically displays, besides the inherent discontinuous displacements, a component of continuous deformation (Barnett et al, 1987; Long & Imber, 2010), manifested by folding of the beds adjacent to the fault surface. These folds are the result of plastic strains or small-scale faulting (Walsh & Watterson, 1991; Walsh et al, 1996) and their generation is attributed to various processes throughout different periods of the fault system evolution, such as fault propagation (Withjack et al, 1990; Schlische, 1995; Ferrill, 2012), interaction of fault segments (Childs et al, 1996; Long & Imber, 2010; Long & Imber, 2012) or frictional drag (Davis & Reynolds, 1984). We study the spatial variability and magnitude of continuous deformation surrounding a normal fault-array with complex 3D geometry within a mechanically heterogeneous Jurassic - Triassic sedimentary sequence from Inner Moray Firth Basin (Figure 1 & 2). We explore the mechanisms by which the geometry of the Late Jurassic - Early Cretaceous syn-sedimentary normal faults controls the spatial variability of normal fault-related ductile deformation.

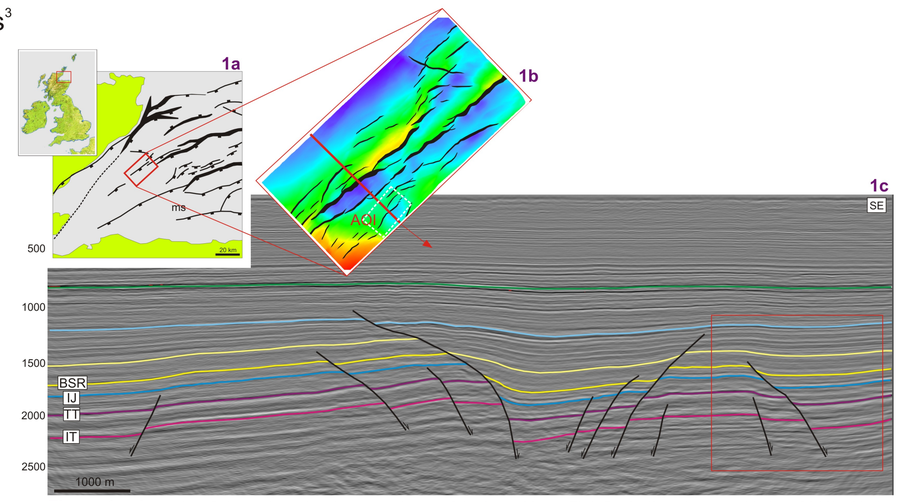

Figure 1 a, b, c. **1a** - Schematic regional structural map of the Inner Moray Firth Basin (from Long and Imber, 2010) with the location of the interpreted 3D seismic volume. **1b** - Top Triassic TWT structural map with the location of the studied fault-array. **1c** - Seismic section orthogonal to the strike of the Jurassic normal faults; the analysed faults are bordered by the red square.

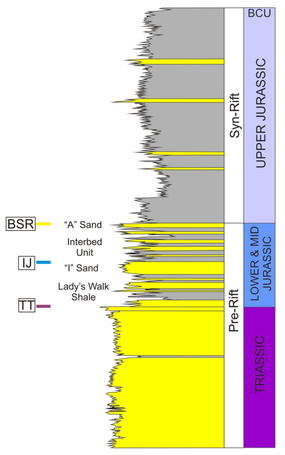

Figure 2. Jurassic-Triassic litho-stratigraphic column from the Beatrice Field.

Methods

We interpret a 3D time-migrated seismic volume and analyse the deformed seismic reflectors adjacent to the normal fault planes. Velocity data from nearby wells do not show significant velocity changes with depth, so the analysis was performed on time data, in order to avoid uncertainties associated with depth conversion. We use the fault-normal rotation method developed by Long and Imber (2010) to analyse the spatial distribution and vertical component of continuous deformation adjacent to a normal fault-array (Figure 3). The dip attribute maps presented here are based on dip attribute extracted for a 25 m cell size of the gridded mapped horizons. The 25 m cell size was chosen because it is a good representation of the raw data (mapped on 12.5 by 12.5 m IL and XL spacing) but also removes some of the potential noise (misinterpretation due to sampling related issues).

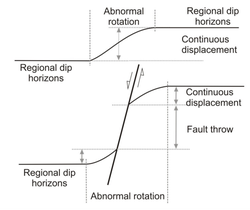

Figure 3. The two measured components of deformation, discontinuous and continuous (from Long & Imber, 2010).

Fault Geometry

Figure 5 shows a 3D representation of the studied *fault segments A*, *B* and *C*. *Faults A* and *B* are two soft-linked segments at Intra-Triassic level, which merge into a main fault segment at near Top Triassic level and splay upwards into en-echelon vertical branched faults at both SW and NE terminations of the fault (Figure 4, 5). All the vertical splays die out in the Mid Jurassic sediments and only a part of the principal segment breaches the Base Syn-Rift marker. The linkage of *segments A* and *B* generates a downward bifurcation which produces a complex undulating surface morphology. This bend in the fault plane depends on the horizontal separation between the two overlapping segments.
Segment C is a fault in the footwall of the main *fault AB*. It has a relatively simple planar geometry.

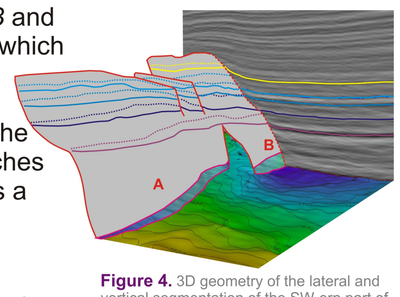

Figure 4. 3D geometry of the lateral and vertical segmentation of the SW-ern part of the fault surface. View towards NE.

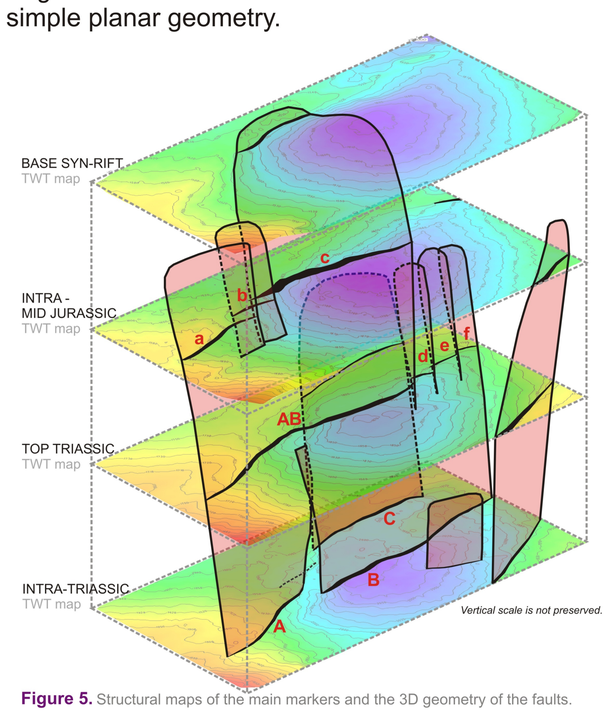

Figure 5. Structural maps of the main markers and the 3D geometry of the faults.

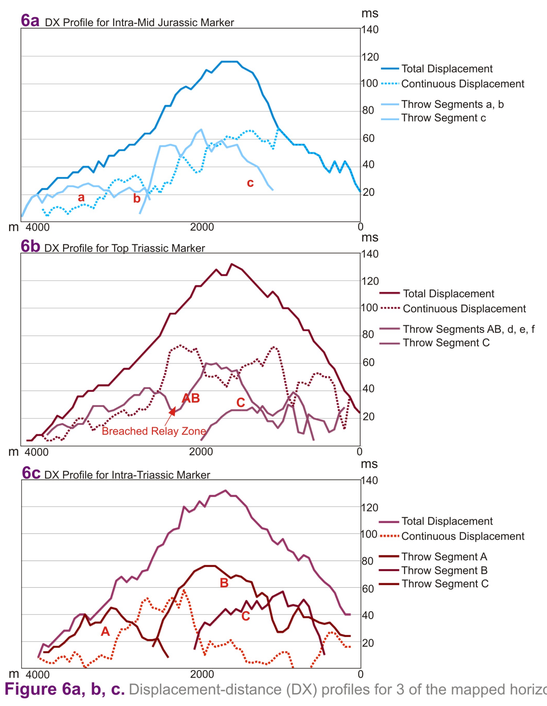

Figure 6a, b, c. Displacement-distance (DX) profiles for 3 of the mapped horizons.

The displacement-distance profiles show the continuous and discontinuous displacement variations on faults A, B and C (Figure 6). It can be observed that the fault-related continuous deformation increases in the vicinity of the interacting faults (relay zones) and added to the aggregate discontinuous component of displacement produces a symmetrically bell-shaped deformation profile, indicating the geometrical coherence of the fault-array.

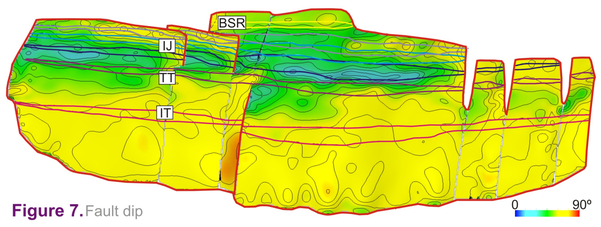

Figure 7. Fault dip

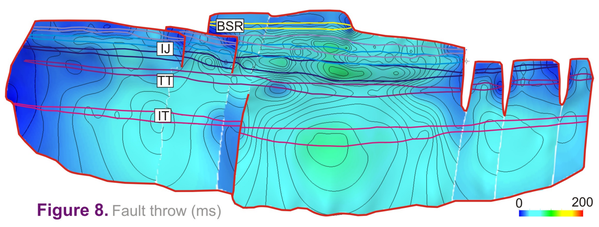

Figure 8. Fault throw (ms)

Figure 7 displays the contoured values of the fault dip on the strike projection of the fault surface. It can be observed a sharp decrease in fault dip above the Top Triassic level which contrasts with the relatively constant fault dip (~60º) at depth. This change in dip corresponds with a major change in lithology, from the Triassic sandstones to the shale-dominated Jurassic sediments (Figure 2). The strike projection of the fault throw (Figure 8) displays a significant decrease in fault throw corresponding with this main mechanical boundary. Vertical en-echelon segmentation may reflect the changes in lithology, where deformation in the more incompetent Jurassic sediments is accommodated by shear failure on multiple surfaces. Displacement maxima within the Intra-Triassic and also within the Intra-Mid Jurassic sediments, suggest that the faults evolved as separate vertical segments, which nucleated in the more competent layers (Triassic sands and Jurassic "I" Sand, see Figure 2). The faults linked developing a contractional bend, expressed by the lower dip of the fault, displacement minima and associated ductile deformation.

Fault-Related Folding

The patterns of abnormal rotation are not uniformly distributed in the volume surrounding the studied normal faults (Figure 9).
Displacement on fault *segment A* is accommodated by rotation of BSR on a 500 m wide zone located above the vertical tips of the *a* and *b splay faults* (Figure 9, S2).
Deformation associated with the *segment b* extends 900m SW from the tip of the fault, generating intense bed rotation of BSR in the FW of *segment a* (Figure 9, S1).
Rotation of TT marker increases in the *relay zone of fault A* and *B* (Figure 6b, Figure 9), where *fault B* develops a convex upward geometry. This type of fault geometry can enhance development of synthetic bed rotation in the HW (S3).
A narrow but pronounced kink of the TT reflector continues linearly SW from the relay zone, above the vertical tip of a possible SW prolongation of *fault B* (S2).
The interaction between *fault C* and *fault B* triggers rotation of the FW of *fault B* so that the deformation of BSR above the tip of the fault is broadly distributed, generating a wide monocline, where strain is accommodated by small scale faulting (Figure 9, S4).

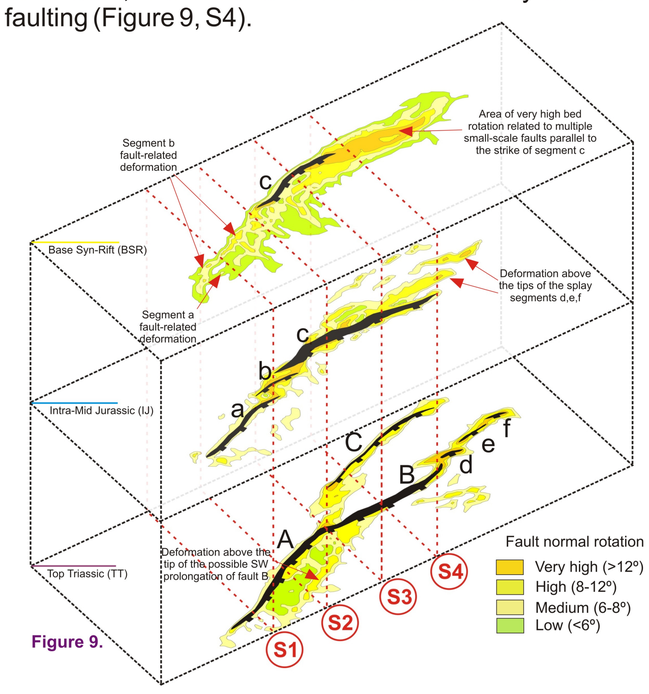

Figure 9.

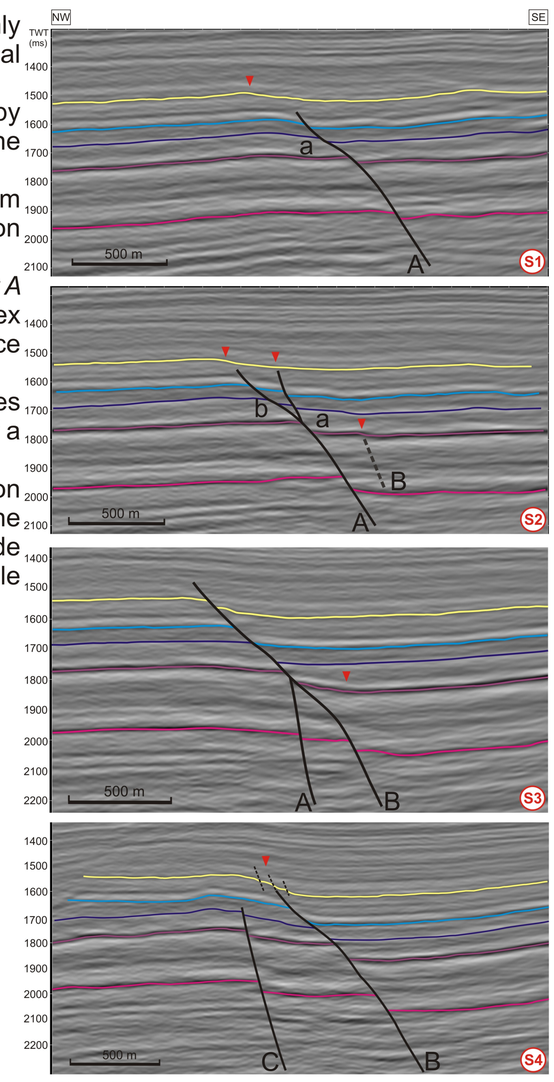

Figure 10. Seismic sections, S1 to S4 (from W to E) through the studied fault-array. Location in Figure 9.

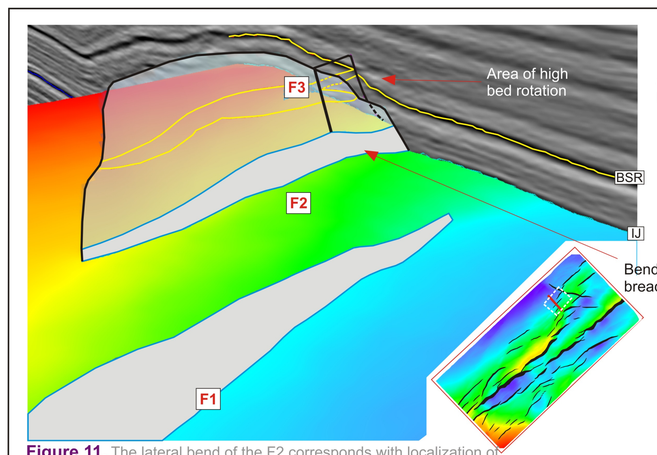

Figure 11. The lateral bend of the F2 corresponds with localization of vertical segmentation of the fault and high fault-normal rotation of BSR.

Vertical segmentation of a fault can produce contractional offsets at lithological boundaries (Childs et al, 1999). The horizontal separation between the vertical fault segments can vary along strike and it is influenced by the lateral linkage of the faults. An increasing horizontal segment separation is associated with higher magnitudes of continuous deformation.

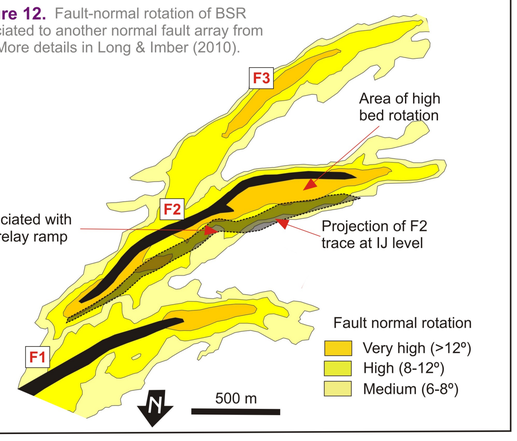

Figure 12. Fault-normal rotation of BSR associated to another normal fault array from IMF. More details in Long & Imber (2010).

Concluding Remarks

Analysis of the fault normal dip data shows that the majority of the fault related folding is localized in the shale-dominated Jurassic sequence.
The largest magnitude of bed rotation is located above or along strike from the upper and lateral fault tips. This confirms the results of Long & Imber, 2010.
The spatial variability and magnitude of ductile deformation along a single complex fault plane can be explained by various contributing processes, such as fault propagation (S1, S2), interaction and linkage of fault segments (Figure 9, S3) and HW translation over an undulatory fault surface (S3). This emphasizes the importance of the fault geometry, in particular lateral (breached relay zones) and vertical bends (contractional steps) on the localization and magnitude variability of continuous deformation along a complex fault zone.

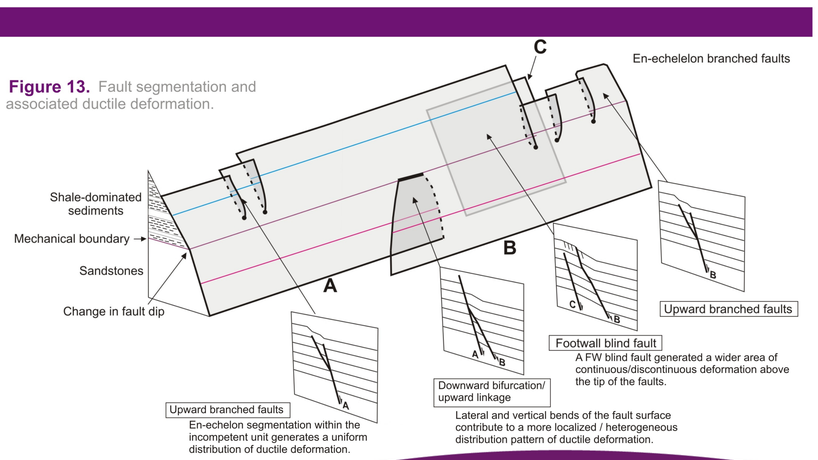

Figure 13. Fault segmentation and associated ductile deformation.

Aknowledgements

We are grateful to Badley Geoscience Ltd. for providing license and training for TrapTester.

References

Barnett, J.A., Mortimer, J., Rippon J.H., Walsh, J.J., Watterson, J., 1987. Displacement geometry in the volume containing a single normal fault. AAPG Bulletin 71, 925-937.
Childs, C., Nicol, A., Walsh, J.J., Watterson, J., 1996a. Growth of vertically segmented normal faults. Journal of Structural Geology 18 (12), 1389–1397.
Davis, G.H., Reynolds, S.J., 1984. Structural geology of rocks and regions. John Willey and Sons,New York, 492 pp.
Ferrill, D.A., Morris, A.P., 2008. Fault zone deformation controlled by carbonate mechanical stratigraphy, Balcones fault system, Texas. AAPG Bulletin 92, 359–380.
Ferrill, D.A., Morris, A.P., McGinnis, R.N. 2012. Extensional fault-propagation folding in mechanically layered rocks: The case against the frictional drag mechanism. Tectonophysics 576-577, 78-85.
Long, J.J., Imber, J., 2010. Geometrically coherent continuous deformation in the volume surrounding a seismically imaged normal fault-array. Journal of Structural Geology 32 (2), 222-234.
Long, J.J., Imber, J., 2012. Strain compatibility and fault linkage in relay zones on normal faults. Journal of Structural Geology 36 (2012) 16-26.
Schlische, R.W., 1995. Geometry and origin of fault-related folds in extensional settings. AAPG Bulletin 79, 1661–1678.
Walsh J.J., Watterson, J.1991. Geometric and kinematic coherence and scale effects in normal fault system. In Roberts, A.M., Yielding, G.,Freeman, B. (Eds.), The Geometry of Normal Faults. Geological Society Special Publications, No. 56, 193-203.
Walsh J.J., Watterson, J., Childs C.,Nicol, A. 1996. Ductile strain effects in the analysis of seismic interpretation of normal faults. In Buchanan, P.G., Nieuwland, D. A. (Eds.), Modern Developments in Structural Interpretation, Validation and Modelling. Geological Society Special Publications, No. 99, 27-40.
Withjack, M.O., Olson, J., Peterson, E., 1990. Experimental models of extensional forced folds. AAPG Bulletin 74, 1038–1054.

Durham University
CeREES
Badleys Badley Geoscience Limited
Petroleum

Seismic imaging of deformation zones associated with normal fault-related folding

Alexandru Lăpădat[1*], Jonathan Imber[1,2], David Iacopini[3], Richard Hobbs[1]

[1]Department of Earth Sciences, Durham University, Durham, DH1 3LE, UK
[2]Badley Geoscience Ltd., Hundleby, Spilsby, Lincolnshire, PE23 5NB, UK
[3]Geology and Petroleum Geology Department, University of Aberdeen, Aberdeen, AB24 3UE, UK

*Corresponding author (e-mail: i.a.lapadat@durham.ac.uk)

Introduction

Displacement on normal faults is often partitioned between numerous slip surfaces and adjacent volumes of deformed rocks, characterized by secondary faulting and intense fracturing. The deformation zone surrounding normal faults can extend for several hundreds of meters from the main fault and is mainly generated by propagation (folding ahead of the propagating fault tip) and linkage (laterally or vertically) of fault segments. Analogue models in clay provide good insights into the complex deformation patterns associated with folding ahead of a propagating normal fault (**Figure 1**) (Withjack et al, 1991). Multiple synthetic splay faults, reverse faults or small antithetic Riedel structures can accommodate a large part of the total displacement, but because the total displacement is partitioned on a dense system of faults with smaller offsets, it is very likely that the deformation would not be imaged by conventional industry seismic reflection data.

Botter et al (2014) performed synthetic seismic imaging of a geomechanical model of distributed deformation surrounding a normal fault and showed that strain related changes in the acoustic properties of the rocks impact the seismic amplitude variations surrounding the fault. Here we test this hypothesis on real seismic data from Inner Moray Firth, offshore Scotland, and explore the possibility that dilation of the rock volume caused by sub-seismic scale faulting and fracturing associated with folding (**Figure 2a**) generates amplitude dimming of the reflections surrounding the normal fault (**Figure 2b**).

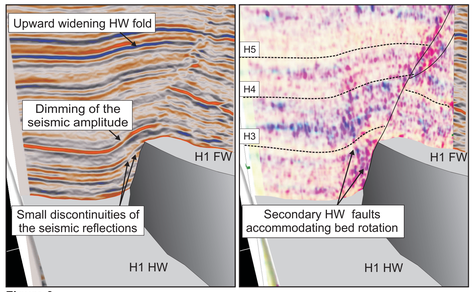

Figure 3
Combined **tensor-semblance-discontinuity** attribute volume enhances visualization of secondary splay faults accommodating HW folding of a normal fault from IMF (similar with **Figure 1**).

Envelope represents the total instantaneous energy of the complex trace, independent of phase.

Instantaneous amplitude (Envelope attribute) shows a decrease in amplitude in the vicinity of the fault, indicating a possible effect of fault-related deformation.

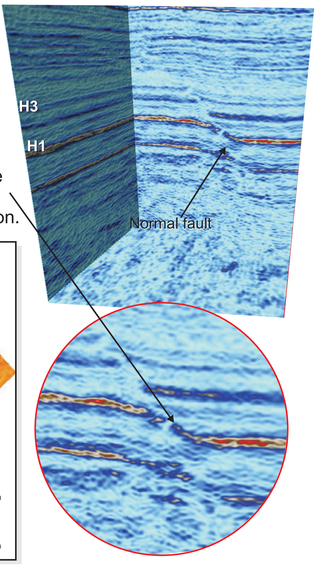

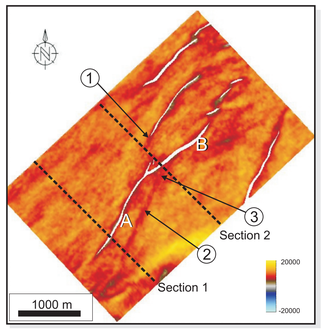

Figure 4

Dimming of seismic amplitude in the vicinity of the faults:
1. Fault tip - decrease in throw (under the seismic resolution)
2. Sub-seismic scale faulting
3. Fault linkage and folded zones

Normal fault deformation zones in:

Analogue and kinematic models of normal fault-related folding

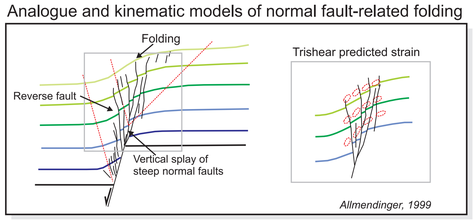

Figure 1

Outcrops

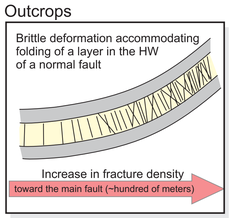

Figure 2a

Reflection seismic data

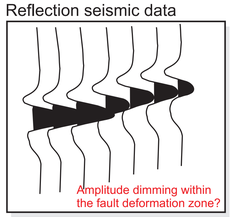

Figure 2b

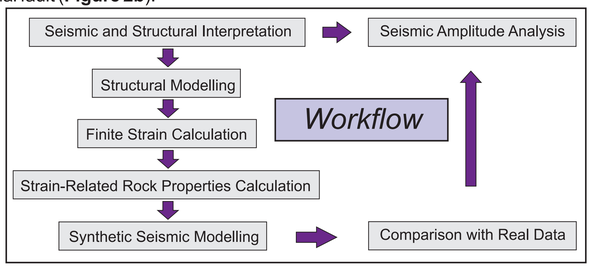

Structural Interpretation & Modelling

We analyse an Upper Jurassic syn-rift fault, cutting through a Triassic sandstone-dominated sequence (pre-H1) capped by a 15 m thick cherty carbonate layer (H1), which is characterized by a distinct, continuous, high amplitude reflector (**Figure 4**) and overlayed by a Lower-Mid Jurassic shale-dominated sequence, interbedded with sandstone layers (H1-H3).The studied fault array (**Figure 5**) comprises a downward bifurcated normal fault, generated by linkage of two lateral segmented normal faults with a shallower segment (**Figure 6**). The lateral and vertical propagation of segments *B* and *C* generates breached monoclinal folds of horizon H1 and H3 (**Figure 6** and **Section 2**).

The folding related to normal faulting was forward modelled to fit the depth converted seismic data (**Figure 7**), using the trishear algorithm in Move software. Regular 20 m spaced points were used to calculate the distribution of strain field (**Figure 8a**), its orientation and magnitude within the deformed section. Kinematic models have no mechanical basis and do not allow area and volumetric change within the deformation zone. However, longitudinal strain magnitude can be used as proxy for fracture intensity and for volumetric changes of the rocks (if we assume a perfect compressible material), because the maximum principal stretch axis (e1) is usually parallel with the beds within the folded area (**Figure 1**).

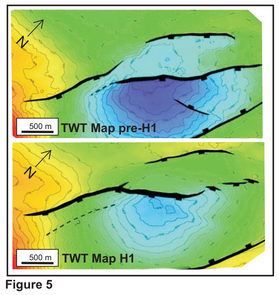

Figure 5

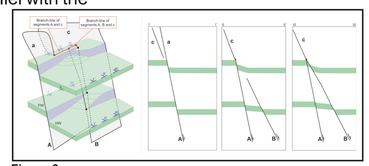

Figure 6

The same 20 m spaced grid was used to calculate strain-related changes of the initial acoustic properties of the rocks (**Figure 8**), using the equations from Botter et al (2014).

Porosity $\Phi = \Phi_{ini}(0.25\ E_V + 1), \quad -1 \le E_V \le 1$

Density $\rho = \rho_g(1-\Phi) + \rho_w\Phi$

Velocity $V_{P\ ini}(0.25E_V^2 - 0.5E_V + 1), \quad 0 \le E_V \le 1 \quad (dilation)$

Strain (*e1*)

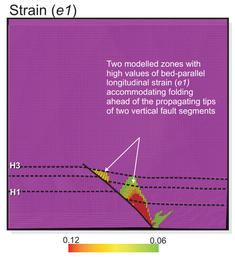

Figure 8a

P-wave velocity (*Vp*)

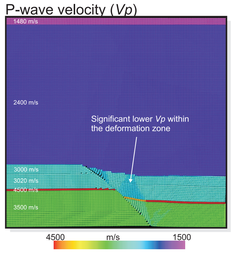

Figure 8b

Density (*ρ*)

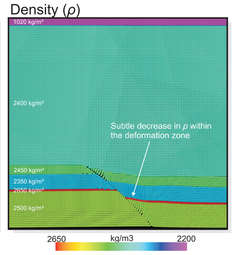

Figure 8c

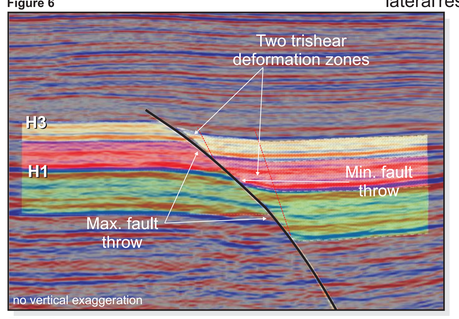

Figure 7

Seismic Amplitude Analysis

Horizon H1 was 3D autotracked along the largest peaks and amplitude values were extracted (**Figure 4**). A mean amplitude was calculated and deviation from this value was plotted for each trace along sampled sections orthogonal on the fault (**Figure 9**). Amplitude variations are minimum within the undeformed part of the footwall (**Section 1** and **2** and **Figure 9**). A small fault can be identified in **Section 1** based on the amplitude reductions associated with small fault offset and liniar continuity of the anomaly (**Figure 4**). Along **Section 2** the bright amplitude is dimming in the proximity of the fault. The amplitude anomaly corresponds with the folded area of marker H1 (**Figure 9**).

Section 1

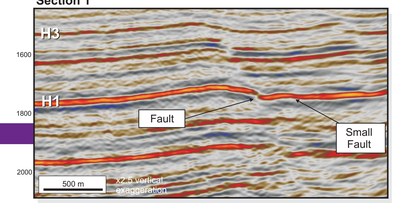

Section 2

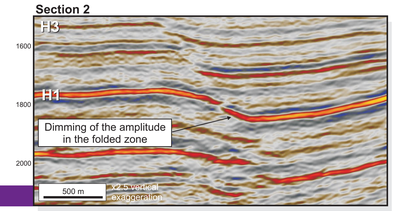

Seismic amplitude variation of H1 along Section 1

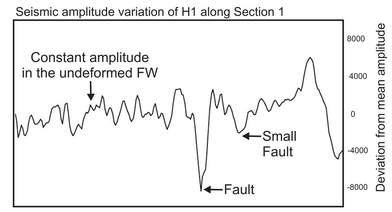

Seismic amplitude variation of H1 along Section 2

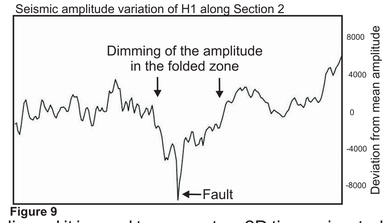

Figure 9

Synthetic Seismic Modelling

Acoustic finite difference modelling code provides a detailed description of 2D wavefields within a complex heterogeneous media and it is used to generate a 2D time-migrated synthetic seismic section based on the provided Vp velocities and density grids (with 20 m sampling points).The type of source signature used is a Ricker wavelet at a frequency of 20 Hz, with 20 m spacing between each shotpoint. The frequency content is constrained by the grid density, so a higher frequency would require denser sampling points. For this study we use the lower 20 Hz frequency only. Even at 20 Hz frequency the modelled synthetic sections show amplitude dimming as a result of changes in velocity and density within the fault zone. Model 1(**Figure 10 a**) which is characterized by a decrease in the acoustic properties of the entire fault zone (even in the shale layers above H1) shows a subtle pull-down effect of reflector H and slightly dimming amplitudes along the H1 HW fold limb. This velocity effect can be potential wrongly interpreted as an antithetic fault. In model 2 (**Figure 10 b**) we consider the shale interval as incompressible, and as a consequence, volumetric changes will not occur, but rather the shales will change shape (will "flow") as a result of plastic strains. This model fits better with the real data from IMF, the geometry and dip of the fold limb is better reproduced and the amplitude reductions are conformant with the deformation zone, similar withe the IMF example. Future work on a higher frequency model would be required to minimise the lateral resolution constrains and to analyse in more detail the strain-related variation of amplitudes.

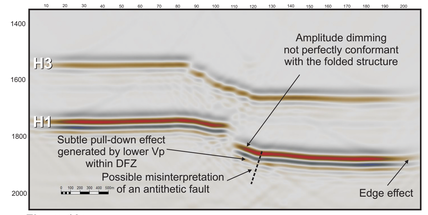

Figure 10a
Model 1 - Strain-related *Vp* and *ρ* changes within all the deformation zone

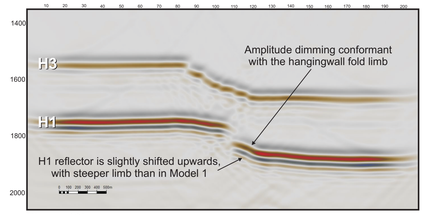

Figure 10b
Model 2 - Strain-related *Vp* and *ρ* changes included only for mechanically competent units (H1 and pre-H1)

Seismic amplitude variation of H1on Synthetic Model 1 and 2

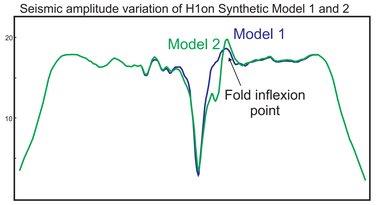

Figure 10c

Aknowledgements
We thank Schlumberger for providing academic license for Petrel, Midland Valley for providing license for Move software and Foster Findlay Associates Ltd. for providing access to GeoTeric software.

References

Allmendinger, R. W. 1999. Trishear research at Cornell. *www.geo.cornell.edu/RWA/trishear/default.html*
Botter, C., Cardozo, N., Hardy, S., Lecomte, I., Escalona, A. 2104. From mechanical modeling to seismic imaging of faults: A synthetic workflow to study the impact of faults on seismic. *Marine and Petroleum Geology* 57, 187-207.
Stockwell, JW., Cohen, J. K. 2008. The New Seismic Unix User's Manual. Colorado School of Mines, Golden, CO, USA, 141 p.
Withjack, M.O., Olson, J., Peterson, E., 1990. Experimental models of extensional forced folds. *AAPG Bulletin* 74, 1038–1054.

Petroleum

Appendix 3

Data	Location	Source	Data type	Lithology	Relay Type / Type of Breaching	Overlap Length (m)	Separation distance (m)	Throw / Separation	Average Ramp Shear Strain	Throw FF (m)	Throw RF (m)	Throw Asymmetry	Breaching Index (Cartwright et al, 1994)
Laminaria	Bonaparte Basin, offshore Australia	This Study	3D Seismic	Carbonates	Breached FW	736	120	0,569	0,063	70,5	66	1,068	92,16
Laminaria	Bonaparte Basin, offshore Australia	This Study	3D Seismic	Carbonates	Intact	280	120	0,344	0,147	51	31,5	1,619	100,00
Laminaria	Bonaparte Basin, offshore Australia	This Study	3D Seismic	Carbonates	Intact	480	225	0,200	0,094	61,5	28,5	2,158	100,00
Laminaria	Bonaparte Basin, offshore Australia	This Study	3D Seismic	Carbonates	Breached FW	560	90	1,033	0,166	121,5	64,5	1,884	87,10
Laminaria	Bonaparte Basin, offshore Australia	This Study	3D Seismic	Carbonates	Breached FW,HW	426	111	0,682	0,178	69	82,5	0,836	92,00
Laminaria	Bonaparte Basin, offshore Australia	This Study	3D Seismic	Carbonates	Breached FW	300	39	0,981	0,128	46,5	30	1,550	86,11
Laminaria	Bonaparte Basin, offshore Australia	This Study	3D Seismic	Carbonates	Intact	992	390	0,121	0,048	46,5	48	0,969	100,00
Laminaria	Bonaparte Basin, offshore Australia	This Study	3D Seismic	Carbonates	Intact	746	222	0,338	0,101	72	78	0,923	100,00
Laminaria	Bonaparte Basin, offshore Australia	This Study	3D Seismic	Carbonates	Intact	564	70	0,814	0,101	58,5	55,5	1,054	100,00
Laminaria	Bonaparte Basin, offshore Australia	This Study	3D Seismic	Carbonates	Intact	1160	80	0,553	0,038	66	22,5	2,933	100,00
Laminaria	Bonaparte Basin, offshore Australia	This Study	3D Seismic	Carbonates	Intact	464	92	0,497	0,099	48	43,5	1,103	100,00
Laminaria	Bonaparte Basin, offshore Australia	This Study	3D Seismic	Carbonates	Breached HW	965	115	0,196	0,023	22,5	22,5	1,000	53,13
Laminaria	Bonaparte Basin, offshore Australia	This Study	3D Seismic	Carbonates	Intact	498	128	0,199	0,051	27	24	1,125	100,00
Laminaria	Bonaparte Basin, offshore Australia	This Study	3D Seismic	Carbonates	Intact	525	318	0,108	0,066	33	36	0,917	100,00
Laminaria	Bonaparte Basin, offshore Australia	This Study	3D Seismic	Carbonates	Breached HW,Mid	524	47	0,415	0,037	15	24	0,625	46,88
Laminaria	Bonaparte Basin, offshore Australia	This Study	3D Seismic	Carbonates	Intact	740	57	0,421	0,032	24	24	1,000	100,00
Laminaria	Bonaparte Basin, offshore Australia	This Study	3D Seismic	Carbonates	Breached FW	300	37	0,689	0,085	27	24	1,125	100,00
Laminaria	Bonaparte Basin, offshore Australia	This Study	3D Seismic	Carbonates	Intact	386	190	0,079	0,039	22,5	7,5	3,000	100,00
Laminaria	Bonaparte Basin, offshore Australia	This Study	3D Seismic	Carbonates	Breached FW	865	107	0,301	0,037	21	43,5	0,483	46,67
Laminaria	Bonaparte Basin, offshore Australia	This Study	3D Seismic	Carbonates	Breached FW	755	260	0,211	0,073	73,5	36	2,042	92,45
Laminaria	Bonaparte Basin, offshore Australia	This Study	3D Seismic	Carbonates	Breached FW	394	101	0,661	0,169	79,5	54	1,472	92,98
Laminaria	Bonaparte Basin, offshore Australia	This Study	3D Seismic	Carbonates	Breached FW	500	40	0,731	0,059	28,5	30	0,950	86,36
Laminaria	Bonaparte Basin, offshore Australia	This Study	3D Seismic	Carbonates	Breached FW	295	38	0,454	0,058	12	22,5	0,533	42,11
Laminaria	Bonaparte Basin, offshore Australia	This Study	3D Seismic	Carbonates	Breached FW	428	50	0,600	0,070	33	27	1,222	40,74
Laminaria	Bonaparte Basin, offshore Australia	This Study	3D Seismic	Carbonates	Breached Mid	525	55	0,436	0,046	21	27	0,778	45,16
Laminaria	Bonaparte Basin, offshore Australia	This Study	3D Seismic	Carbonates	Intact	475	50	0,285	0,030	16,5	12	1,375	100,00
Laminaria	Bonaparte Basin, offshore Australia	This Study	3D Seismic	Carbonates	Intact	543	55	0,614	0,062	52,5	15	3,500	100,00
Laminaria	Bonaparte Basin, offshore Australia	This Study	3D Seismic	Carbonates	Breached FW	376	37,5	1,080	0,108	38,25	42,75	0,895	72,86
Laminaria	Bonaparte Basin, offshore Australia	This Study	3D Seismic	Carbonates	Intact	562	55	0,389	0,038	28,5	14,25	2,000	100,00
Laminaria	Bonaparte Basin, offshore Australia	This Study	3D Seismic	Carbonates	Breached FW	250	65	0,346	0,090	24	21	1,143	72,73
Laminaria	Bonaparte Basin, offshore Australia	This Study	3D Seismic	Carbonates	Intact	383	55	0,607	0,087	43,5	23,25	1,871	100,00
Laminaria	Bonaparte Basin, offshore Australia	This Study	3D Seismic	Carbonates	Breached Mid	702	50	1,020	0,073	61,5	40,5	1,519	66,13
Laminaria	Bonaparte Basin, offshore Australia	This Study	3D Seismic	Carbonates	Breached FW	830	220	0,338	0,089	84	64,5	1,302	90,32
Laminaria	Bonaparte Basin, offshore Australia	This Study	3D Seismic	Carbonates	Intact	810	110	0,743	0,101	75	88,5	0,847	100,00
Laminaria	Bonaparte Basin, offshore Australia	This Study	3D Seismic	Carbonates	Breached	1025	110	0,661	0,071	76,5	69	1,109	92,73
Laminaria	Bonaparte Basin, offshore Australia	This Study	3D Seismic	Carbonates	Breached FW	419	40	1,969	0,188	76,5	81	0,944	87,93
Laminaria	Bonaparte Basin, offshore Australia	This Study	3D Seismic	Carbonates	Breached HW	700	40	0,375	0,021	108	15		12,20
Laminaria	Bonaparte Basin, offshore Australia	This Study	3D Seismic	Carbonates	Breached HW	640	65	0,715	0,073	40,5	46,5		53,45
Laminaria	Bonaparte Basin, offshore Australia	This Study	3D Seismic	Carbonates	Breached HW	395	40	1,050	0,106	27	42		60,87
Laminaria	Bonaparte Basin, offshore Australia	This Study	3D Seismic	Carbonates	Breached HW	965	115	0,222	0,026	22,5	25,5		53,13
Laminaria	Bonaparte Basin, offshore Australia	This Study	3D Seismic	Carbonates	Breached HW	320	70	0,257	0,056	84	18		17,65
Laminaria	Bonaparte Basin, offshore Australia	This Study	3D Seismic	Carbonates	Breached HW	405	47	0,319	0,037	3	15		83,33
Chandon	Carnarvon Basin, offshore Australia	This Study	3D Seismic	Shales-sandstones	Intact	595	205	0,223	0,077	45	46,5	0,968	
Chandon	Carnarvon Basin, offshore Australia	This Study	3D Seismic	Shales-sandstones	Breached Mid	280	80	1,566	0,447	127,5	123	1,037	
Chandon	Carnarvon Basin, offshore Australia	This Study	3D Seismic	Shales-sandstones	Intact	705	240	0,334	0,114	64,5	96	0,672	
Chandon	Carnarvon Basin, offshore Australia	This Study	3D Seismic	Shales-sandstones	Intact	455	218	0,138	0,066	37,5	22,5	1,667	
Chandon	Carnarvon Basin, offshore Australia	This Study	3D Seismic	Shales-sandstones	Intact	425	335	0,128	0,101	55,5	30	1,850	
Chandon	Carnarvon Basin, offshore Australia	This Study	3D Seismic	Shales-sandstones	Intact	150	145	0,243	0,235	36	34,5	1,043	
Chandon	Carnarvon Basin, offshore Australia	This Study	3D Seismic	Shales-sandstones	Intact	745	153	0,951	0,195	172,5	118,5	1,456	
Chandon	Carnarvon Basin, offshore Australia	This Study	3D Seismic	Shales-sandstones	Intact	1402	720	0,083	0,043	49,5	70,5	0,702	
Chandon	Carnarvon Basin, offshore Australia	This Study	3D Seismic	Shales-sandstones	Intact	2450	630	0,363	0,093	226,5	231	0,981	
Chandon	Carnarvon Basin, offshore Australia	This Study	3D Seismic	Shales-sandstones	Breached FW	835	225	1,830	0,493	432	391,5	1,103	
Inner Moray Firth	Northern North Sea, offshore UK	This Study	3D Seismic	Shales-sandstones	Breached FW, Mid, H	737,5	240	0,659	0,215	150	166,5	0,901	
Inner Moray Firth	Northern North Sea, offshore UK	This Study	3D Seismic	Shales-sandstones	Intact	800	400	0,293	0,146	79,5	154,5	0,515	
Inner Moray Firth	Northern North Sea, offshore UK	This Study	3D Seismic	Shales-sandstones	Intact	450	350	0,737	0,573	357	159	2,245	
Inner Moray Firth	Northern North Sea, offshore UK	This Study	3D Seismic	Shales-sandstones	Breached FW	812	350	0,379	0,163	141	124,5	1,133	
Inner Moray Firth	Northern North Sea, offshore UK	This Study	3D Seismic	Shales-sandstones	Breached FW	700	650	0,308	0,286	300	100,5	1,704	
Inner Moray Firth	Northern North Sea, offshore UK	This Study	3D Seismic	Shales-sandstones	Intact	1025	370	0,119	0,043	56,25	31,5	1,786	
Inner Moray Firth	Northern North Sea, offshore UK	This Study	3D Seismic	Shales-sandstones	Intact	1100	305	0,334	0,093	123	81	1,519	
Miskar Field	Gulf of Gabes, offshore Tunisia	This Study	3D Seismic	Carbonates	Intact	5900	1250	0,089	0,019	84	138	0,609	
Miskar Field	Gulf of Gabes, offshore Tunisia	This Study	3D Seismic	Carbonates	Intact	2210	530	0,232	0,056	123	123	1,000	
Miskar Field	Gulf of Gabes, offshore Tunisia	This Study	3D Seismic	Carbonates	Intact	660	1035	0,049	0,077	67,5	34,5	1,957	

Miskar Field	Gulf of Gabes, offshore Tunisia	This Study	3D Seismic	Carbonates	Intact		4050	1220	0,116	0,035	126	156	0,808
Parihaka Fault	Taranaki Basin, offshore New Zealand	This Study	3D Seismic	Shales-sandstones	Intact		2275	1375	0,115	0,070	172	145	1,186
Parihaka Fault	Taranaki Basin, offshore New Zealand	This Study	3D Seismic	Shales-sandstones	Intact		2482	1565	0,055	0,035	52	121	0,430
Daisy Hill	Northumberland, UK	Huggins,1995	Field	Coals	Intact		161	69,5	0,172	0,074	11,7	12,2	0,959
Plenmellor 1 Main	Northumberland, UK	Huggins,1995	Field	Coals	Intact		7	2,98	0,898	0,382	2,2	3,15	0,698
Barnsley Seam, Silverwood Colliery	South Yorkshire, UK	Huggins,1995	Mine plans	Coals	Intact		416	83	0,042	0,008	4,2	2,7	1,556
Slikstone Seam, Rockingham Colliery	South Yorkshire, UK	Huggins,1995	Mine plans	Coals	Intact		60	10	0,081	0,014	0,8	0,82	0,976
Parkgate Seam, Denaby Main, Colliery	South Yorkshire, UK	Huggins,1995	Mine plans	Coals	Intact		11,75	11,75	0,115	0,115	1,5	1,2	1,250
1st Waterloo Seam, Silverwood Colliery	South Yorkshire, UK	Huggins,1995	Mine plans	Coals	Intact		39	22	0,042	0,024	1,1	0,75	1,467
2nd Waterloo Seam, Silverwood Colliery	South Yorkshire, UK	Huggins,1995	Mine plans	Coals	Intact		132	15	0,097	0,011	1,05	1,85	0,568
Plenmellor Opencast Coal Site	Northumberland, UK	Huggins,1995	Field	Coals	Intact		2,3	1,2	0,958	0,288	0,7	1,6	0,438
Plenmellor Opencast Coal Site	Northumberland, UK	Huggins,1995	Field	Coals	Intact		1	0,46	1,304	0,341	0,8	0,4	2,000
Plenmellor Opencast Coal Site	Northumberland, UK	Huggins,1995	Field	Coals	Intact		4,9	1,8	0,750	0,540	1,35	1,35	1,000
Plenmellor Opencast Coal Site	Northumberland, UK	Huggins,1995	Field	Coals	Intact		7	2,98	0,898	0,295	2,2	3,15	0,698
Plenmellor Opencast Coal Site	Northumberland, UK	Huggins,1995	Field	Coals	Intact		2,5	0,8	1,250	0,400	1	1	1,000
Potato Pot Opencast Coal Site	Cumbria, UK	Huggins,1995	Field	Coals	Intact		160	80	0,944	0,280	78	73	1,068
Pegswood Opencast Coal Site	Northumberland, UK	Huggins,1995	Field	Coals	Intact		8	4	1,113	0,356	4,8	4,1	1,171
West Chevington Mine	Northumberland, UK	Huggins,1995	Mine plans	Coals	Intact		12,7	8,5	0,147	0,156	1,2	1,3	0,923
West Chevington Mine	Northumberland, UK	Huggins,1995	Mine plans	Coals	Intact		350	73	0,226	0,085	14	19	0,737
Potato Pot Opencast Coal Site	Cumbria, UK	Huggins,1995	Field	Coals	Intact		160	80	0,944	0,280	78	73	1,068
Bishop, Volcanic Tablelands	California, USA	Willemse, 1997	Field	Volcanics	Intact		53	30,5	0,135	0,064	6,17	2,04	3,025
Bishop, Volcanic Tablelands	California, USA	Willemse, 1997	Field	Volcanics	Intact		9	11,6	0,542	0,310	6,47	6,1	1,061
Bishop, Volcanic Tablelands	California, USA	Willemse, 1997	Field	Volcanics	Intact		17	10,5	0,538	0,201	5,8	5,49	1,056
Bishop, Volcanic Tablelands	California, USA	Willemse, 1997	Field	Volcanics	Intact		12	9,7	0,555	0,210	5,3	5,47	0,969
Bishop, Volcanic Tablelands	California, USA	Willemse, 1997	Field	Volcanics	Intact		7	6	0,242	0,097	0,8	2,1	0,381
Bishop, Volcanic Tablelands	California, USA	Dawers & Anders, 1995	Field	Volcanics	Intact		1090	250	0,194	0,049	52	45	1,156
Bishop, Volcanic Tablelands	California, USA	Dawers & Anders, 1995	Field	Volcanics	Intact		910	450	0,163	0,082	95	52	1,827
Bishop, Volcanic Tablelands	California, USA	Dawers & Anders, 1995	Field	Volcanics	Intact		500	60		0,123	90	50	1,800
Bishop, Volcanic Tablelands	California, USA	This Study	Topographic Data	Volcanics	Intact		65	20	0,380	0,117	7,6	5,8	1,310
Bishop, Volcanic Tablelands	California, USA	This Study	Topographic Data	Volcanics	Intact		300	140	0,095	0,049	14,6	12	1,217
Bishop, Volcanic Tablelands	California, USA	This Study	Topographic Data	Volcanics	Intact		1225	174	0,098	0,026	18	16	1,125
Surprise Valley	California, USA	This Study	Topographic Data	Volcanics	Intact		565	210	0,267	0,106	60	52	1,154
Surprise Valley	California, USA	This Study	Topographic Data	Volcanics	Intact		560	198	0,241	0,091	51	44,5	1,146
Surprise Valley	California, USA	This Study	Topographic Data	Volcanics	Breached	FW	335	75	0,572	0,173	65	20,8	3,125
Peter Creek Ramp	Oregon, USA	Crider and Pollard,1998	Field	Volcanics	Intact		750	300	0,203	0,081	61	61	1,000
South Devil's Lane, East Side	Utah, USA	Cartwright, 1996	Field	Sandstones	Intact		345	165	0,515	0,246	80	90	0,889
South Devil's Lane, West Side	Utah, USA	Cartwright, 1996	Field	Sandstones	Intact		206	125	0,588	0,357	70	77	0,909
South Devil's Lane, East Side at Strea Wash	Utah, USA	Cartwright, 1996	Field	Sandstones	Intact		310	83	0,705	0,189	60	57	1,053
Delicate Arch	Utah, USA	Rotevatn, 2007	Field	Sandstones	Intact		431	128	0,352	0,104	45	45	1,000
Hammam Faraun	Suez, Egypt	Bastensen and Rotevatn, 2012	Field	Shales-sandstones	Breached	Mid	135	60	1,167	0,519	40	100	0,400
Kilve	Somerset, UK	Peacock and Sanderson, 1994	Field	Carbonates	Intact		0,75	0,078	0,535	0,056	0,0405	0,043	0,942
Kilve	Somerset, UK	Peacock and Sanderson, 1994	Field	Carbonates	Breached	FW	0,326	0,03	0,900	0,083	0,027	0,027	1,000
Kilve, Fig 2	Somerset, UK	Peacock and Sanderson, 1994	Field	Carbonates	Breached	Mid	0,9	0,12	0,321	0,043	0,042	0,035	1,200
Kilve, Fig 7b	Somerset, UK	Peacock and Sanderson, 1994	Field	Carbonates	Breached	FW, HW?	1,19	0,24	0,189	0,038	0,0495	0,041	1,207
Fumanya F19	Spain	Soliva and Benedicto, 2004	Field	Carbonates	Intact		0,4914	0,25	0,152	0,077	0,024	0,052	0,462
Fumanya F14	Spain	Soliva and Benedicto, 2004	Field	Carbonates	Intact		2,45	1,1	0,114	0,051	0,12	0,13	0,923
Fumanya F10	Spain	Soliva and Benedicto, 2004	Field	Carbonates	Intact		0,19	0,09	0,317	0,150	0,03	0,027	1,111
NIguelas N18	Spain	Soliva and Benedicto, 2004	Field	Carbonates	Intact		0,04	0,012	0,150	0,045	0,0019	0,0017	1,118
Niguelas N21	Spain	Soliva and Benedicto, 2004	Field	Carbonates	Intact		0,716	0,19	0,268	0,071	0,048	0,054	0,889
Niguelas N5	Spain	Soliva and Benedicto, 2004	Field	Carbonates	Intact		4,72	1	0,125	0,026	0,11	0,14	0,786
Fumanya F1	Spain	Soliva and Benedicto, 2004	Field	Carbonates	Breached	Mid	0,382	0,09	0,411	0,097	0,034	0,04	0,850
Fumanya F5	Spain	Soliva and Benedicto, 2004	Field	Carbonates	Breached	HW	0,88	0,12	0,958	0,131	0,07	0,16	0,438
Fumanya F7	Spain	Soliva and Benedicto, 2004	Field	Carbonates	Breached	Mid	1,76	0,4	0,550	0,125	0,22	0,22	1,000
Fumanya F9	Spain	Soliva and Benedicto, 2004	Field	Carbonates	Breached	Mid	1,17	0,22	0,341	0,064	0,1	0,05	2,000
Niguelas N2	Spain	Soliva and Benedicto, 2004	Field	Carbonates	Breached	Mid, HW,	0,915	0,2	0,575	0,126	0,05	0,18	0,278
Fumanya N3	Spain	Soliva and Benedicto, 2004	Field	Carbonates	Breached	HW, Mid	4,451	0,5	0,390	0,044	0,21	0,18	1,167
Relay F6	Spain	Soliva and Benedicto, 2004	Field	Carbonates	Breached	FW	0,261	0,025	2,040	0,195	0,051	0,051	1,000
Lamberton	Northumberland, UK	Long, 2011	Field	Sandstones	Intact		1,785	0,38	0,342	0,073	0,12	0,14	0,857
Lamberton	Northumberland, UK	Long, 2011	Field	Sandstones	Breached	FW	2,611	0,357	0,346	0,047	0,117	0,13	0,900
Lamberton	Northumberland, UK	Long, 2011	Field	Sandstones	Intact		1,061	0,274	0,241	0,062	0,057	0,075	0,760
Lamberton	Northumberland, UK	Long, 2011	Field	Sandstones	Intact		1,098	0,076	1,263	0,087	0,077	0,115	0,670
Lamberton	Northumberland, UK	Long, 2011	Field	Sandstones	Intact		0,628	0,079	0,703	0,088	0,055	0,056	0,982
Lamberton	Northumberland, UK	Long, 2011	Field	Sandstones	Intact		0,964	0,159	0,648	0,107	0,016	0,19	0,084
Runswick Bay RR1	North Yorkshire, UK	This Study	Field	Carbonates	Intact		1,74	0,135	0,656	0,051	0,085	0,092	0,924
Runswick Bay RR2	North Yorkshire, UK	This Study	Field	Carbonates	Intact		0,215	0,04	0,300	0,056	0,012	0,012	1,000
Runswick Bay RR2	North Yorkshire, UK	This Study	Field	Carbonates	Intact		2,75	0,2	0,100	0,007	0,02	0,02	1,000